



Preparation of phosphated Zr-doped TiO₂ exhibiting high photocatalytic activity through calcination of ligand-capped nanocrystals

Sue-min Chang^{*}, Chieh-yao Hou, Pin-han Lo, Chen-tuan Chang

Institute of Environmental Engineering, National Chiao Tung University, 75, Po Ai Street, Hsinchu 30068, Taiwan

ARTICLE INFO

Article history:

Received 8 October 2008

Received in revised form 9 February 2009

Accepted 5 March 2009

Available online 19 March 2009

Keywords:

Co-doping

Phosphated

Zr-doped TiO₂

High photocatalytic activity

Bisphenol A

ABSTRACT

We incorporated phosphate and pyrophosphate species into the surface lattice of Zr-doped TiO₂ via calcination (>550 °C) of triocylphosphine oxide (TOPO)-capped nanocrystals that had been prepared using a non-hydrolytic sol–gel method. The phosphated Zr-doped TiO₂ calcined at 550–750 °C exhibited 2.88–5.28-fold higher photocatalytic activities for decomposition of bisphenol A (BPA) than did P25. Moreover, the sample prepared through calcination at 950 °C performed an extraordinary activity which was 40.3 times higher than that of P25. The high surface reactivities were resulted from co-doping of TiO₂ surface with Zr⁴⁺ and phosphate/pyrophosphate species. Calcination enhanced the reactivity at elevated temperatures because it changed the microstructures and surface properties of phosphated Zr-doped TiO₂. The average crystallite size increased dramatically from 10.2–10.8 to 16.1 nm when the temperature increased from 750 to 950 °C. This change was associated with the formation of pyrophosphate species through condensation of the concentrated phosphate species. Dehydration resulted in substantial amounts of oxygen vacancies ($O_M/M_S = 1.38$) and Ti³⁺ ions in the surface layers of the phosphated Zr-doped TiO₂ calcined at 950 °C. The dehydrated TiO₂ displayed high affinity toward BPA with a maximum adsorption capacity of 5.35 mg/g. The appearance of signals for Ti⁴⁺–O₂[−] in the EPR spectrum of the modified TiO₂ in the dark indicated its high capability for the chemisorption of O₂. In addition, the remarkable decrease in the intensities of trapped electrons in the sample under an O₂ atmosphere revealed that efficient charge transfer occurred from the trapped sites to the electron scavenger. Thus, the phosphated Zr-doped TiO₂ calcined at high temperatures exhibit improved adsorbability toward reactants and enhanced interfacial charge transfer, resulting in outstanding photocatalytic activity.

© 2009 Elsevier B.V. All rights reserved.

1. Introduction

Titanium dioxide (TiO₂)-based photocatalysis is a promising green technology for the efficient oxidization of organic pollutants or the reduction of CO₂ to high potential organics under solar irradiation [1,2]. The incorporation of impurities into TiO₂ lattices has been demonstrated to enhance the photocatalytic activity because it introduces additional energy levels and defects into the electronic structures and microstructures of the TiO₂, respectively. Such influences are mainly associated with the improved interfacial charge transfer, inhibited charge recombination, reduced activation energy, enhanced thermal stability and increased surface acidity [3,4].

The positions of the energy levels of dopants determine their contributions to the photocatalytic activity. Dopants that have energy levels between the conduction and valence bands act as

charge recombination centers and are detrimental to the photocatalytic performance of TiO₂ [5]. Zirconium ions with unoccupied 4d states above the conduction-band minimum of TiO₂ have been demonstrated to improve the photocatalytic activity. Lukáč et al. [6] reported that Zr-doped TiO₂ calcined at 900 °C exhibited a 1.5-fold higher photoactivity than did P25 TiO₂ for the decomposition of 4-chlorophenol because of preferential electron trapping on Zr⁴⁺ rather than on Ti⁴⁺. A P⁵⁺ ion is an alternative dopant which contains its unoccupied 3d states located at the lower energy range of the valence band of TiO₂ [7]. Phosphation of TiO₂ as a means for improving photocatalytic activity has attracted much attention recently. This behavior arises primarily from increased surface acidity and thermal stability [4,8,9]. The superacidity of phosphated TiO₂ promotes the generation of hydroxyl radicals for rapid redox reaction during photocatalysis [10]. In addition, the formation of amorphous titanium phosphate inhibits the coalescence of TiO₂ crystals and prevents the mesoporous structures from undergoing shrinkage of the pore channels during thermal treatment [4]. Thus, phosphation maintains crystallite sizes, leads to high surface areas and retards anatase-to-rutile phase

^{*} Corresponding author. Tel.: +886 3 5712121x55506.

E-mail address: chang@mail.nctu.edu.tw (S.-m. Chang).

transformations all of which favor high photocatalytic activity of TiO_2 [9].

In addition to energy levels, the locations of dopants in the TiO_2 lattice also govern the quantum efficiency of the samples [5]. Effective diffusion and interfacial transfer of charges are the two basic requirements for high quantum efficiency. Charges trapped by bulk defects rarely diffuse to the surface to participate in redox reactions. In contrast, surface defects are beneficial to photocatalytic activity, especially for the samples having nanoscale sizes, because they not only retard charge recombination by trapping but also mediate charge transfer to surface reactants for efficient photocatalysis. Previously, we have successfully incorporated Zr^{4+} ions into the surface lattice of TiO_2 nanocrystals using a non-hydrolytic sol–gel (NHSG) method [3]. This surface doping was resulted from the slow kinetics of condensation between the precursors of ZrO_2 . Meanwhile, the capping agent in the NHSG reaction, trioctylphosphine oxide (TOPO), became chemically bonded to the TiO_2 surface either through complexation or formation of Ti–O–P bonds. The TOPO-capped TiO_2 having a surface Zr-to-Ti ratio of 0.05 exhibited 10-fold higher photocatalytic activity than that of pure TiO_2 , presumably because of the presence of surface defects and the organic modifier.

In this study, we introduced phosphate and pyrophosphate species into the Zr-doped TiO_2 surface lattice through calcination of the TOPO-capped nanocrystals. To understand the phosphorylation process, we examined the effect of calcination temperature on surface chemical compositions and functional groups. In addition, thermal induced changes in the microstructure and optical properties were characterized. The photocatalytic activity of the phosphorylated Zr-doped TiO_2 calcined at various temperatures was monitored in terms of the decomposition of BPA. The effects of the surface properties and the microstructures on the photocatalytic activities were elucidated in terms of the sorption behavior toward reactants and the degree of interfacial charge transfer. BPA is an endocrine disrupting chemical that is potentially carcinogenic and is not decomposed effectively by biological treatment. Understanding the photocatalytic performance of the phosphorylated Zr-doped TiO_2 toward the decomposition of BPA is not only of scientific interests but also of industrial and medicinal importance.

2. Experimental

2.1. Preparation of phosphorylated Zr-doped TiO_2

Phosphorylation of Zr-doped TiO_2 was performed by calcination of ligand-capped nanocrystals that had been prepared through condensation between titanium tetrachloride (TiCl_4 , Fluka, 99%) and zirconium isopropoxide propanol complex ($\text{Zr}(\text{OC}_3\text{H}_7)_4 \cdot (\text{CH}_3)_2\text{CHOH}$, Aldrich, 99.9%) in the presence of TOPO (Fluka, >98%). The TiCl_4 (0.5 g, 2.5 mmol) and $\text{Zr}(\text{OC}_3\text{H}_7)_4 \cdot (\text{CH}_3)_2\text{CHOH}$ (0.8 g, 2.0 mmol) were first dissolved in molten TOPO (5.2 g, 13.5 mmol) at 150 °C under a N_2 atmosphere. The well-mixed solution was then heated at 400 °C and underwent the condensation reaction at this temperature for 3 h with vigorous stirring at 500 rpm. The yellow precursor solution gradually turned to opaque grey during this heating process, indicating the formation of Zr-doped TiO_2 particles. The solution was cooled to 60 °C, and then acetone was added to precipitate the nanoparticles. The precipitate was harvested through centrifugation at 11,000 rpm and washed with acetone several times to remove excess TOPO. Phosphorylated Zr-doped TiO_2 was obtained after further calcination of the TOPO-capped nanoparticles at various temperatures in air for 3 h.

2.2. Characterization

The thermal behavior of the TOPO-capped TiO_2 was investigated by a thermal gravimeter (TG, Seiko SSC 5000) and a differential scanning calorimeter (DSC, Setaram Labsys DSC 131) operated under an air flow of 50 ml/min and at a heating rate of 10 °C/min from 25 to 1000 °C. The surface compositions and chemical states were determined by an X-ray photoelectron spectrometer (XPS, Physical Electronics, ESCA PHI 1600) equipped with an Al $\text{K}\alpha$ X-ray source (1486.6 eV). The photoelectrons were collected into the analyzer with a passing energy of 23.5 eV. The collection step for the wide-ranged scan was 1.0 eV, and it was 0.1 eV for high-resolution analysis in selected energy intervals. All the analytical processes were carried out under ultra-high vacuum conditions which maintained below 1.4×10^{-9} Torr. The surface elemental ratios were estimated from the integrated peak areas of elements normalized by their sensitivity factors. The bulk compositions (Zr/Ti and P/Ti) of the phosphorylated Zr-doped TiO_2 were analyzed by an inductively coupled plasma-mass spectrometer (ICP-MS, Perkin Elmer, SCIEX ELAN 5000). The functional groups of the nanoparticles were identified by a Fourier-transformed infrared spectrometer (FTIR, Horiba FT-720) scanning from 400 to 4000 cm^{-1} . The particle sizes and grain shapes of the phosphorylated Zr-doped TiO_2 were characterized by a high-resolution transmission electron microscope (HRTEM, JEOL JEM-4000EX) operated at an accelerating voltage of 400 kV. The crystalline structures of the phosphorylated Zr-doped TiO_2 were examined by an X-ray diffractometer (XRD, MAC MXP18) using Cu $\text{K}\alpha$ radiation ($\lambda = 1.5405$ Å) and operated at an accelerating voltage of 30 kV and an emission current of 20 mA. The X-ray diffraction patterns were acquired over the 2θ range from 20° to 90° at a sampling width of 0.02° and a scanning speed of 4°/min. Nitrogen adsorption isotherms were measured at 77 K using a N_2 adsorption analyzer (Micromeritics, ASAP 2020). The Brunauer, Emmett, and Teller (BET) model was used to estimate the surface area of the samples according to the N_2 adsorption data. The optical properties and band gaps of the phosphorylated particles were determined using a UV–vis spectrometer (Hitachi, 3010) scanning from 800 to 190 nm.

2.3. Photocatalytic activities

BPA was selected as the target compound. Its degradation rate constants were determined to understand the photoactivity of the phosphorylated Zr-doped TiO_2 . The photocatalysts were suspended in BPA solutions (20 $\mu\text{g/l}$) in the dark to give a final dosage of 1 g/l. Prior to the illumination, the solutions were purged with O_2 for 30 min to ensure the equilibrium among the catalysts, BPA, and oxygen. Photocatalysis was carried out in a fused-silica tube irradiated with UV light at a wavelength of 305 nm. The photocatalytic degradation of BPA solutions was analyzed by high performance liquid chromatograph (HPLC, Waters Alliance 2695) equipped with a C18 column (5 μm , 4.6 mm \times 250 mm) and a photodiode array detector (PDA, Waters 2996, 190–400 nm). The mobile phase was a methanol–water mixture (50/50, v/v) at a flow rate of 1.0 ml/min.

2.4. Dark adsorptions of BPA

Batch sorption equilibria were conducted in the dark at room temperature using 8 ml PTFE-lined screw-cap glass vials. Suspensions were prepared by mixing 5 ml BPA solutions of various concentrations with TiO_2 under vigorous stirring. The dosage of TiO_2 in each batch tests was kept at 1 g/l. After mixing for 30 min, the slurry was centrifuged at 15,000 rpm for 3 min to remove the photocatalysts. The equilibrium concentrations of bisphenol A in the supernatant were measured using HPLC.

2.5. Electron paramagnetic resonance spectroscopy

The photo-induced charge carriers were examined by an electron paramagnetic resonance spectrometer (EPR, Bruker EMX-10) working at X-band frequency. A 500 W Xe lamp (Ushio Inc.) having a major output wavelength at 365 nm was positioned at a fixed distance from a sample cavity. To remove physisorbed water, all samples were heated and evacuated at 120 °C for 1 h in the sealed sample tubes. The measurements were carried out in the vacuumed condition at 77 K either in the dark or under illumination. Subsequently, the same cavities were fully filled with O₂ and again illuminated with UV to examine the trapped charges under an O₂ atmosphere. The instrumental conditions were set at a center field of 3422.5 G and a sweep width of 200.0 G. The microwave frequency was 9.5 GHz and the power was 20 mW.

3. Results and discussion

3.1. Zirconium-doped TiO₂ capped with TOPO

The Zr-doped TiO₂ nanocrystals were prepared by cross condensation between TiCl₄ and Zr(OC₃H₇)₄·(CH₃)₂CHOH in the presence of TOPO at 400 °C. The detailed procedure has been described previously [3]. The Zr-doped TiO₂ was formed as single-crystalline nanorods in length and width of ca. 23.0 and 8.3 nm, respectively (Fig. 4a). The anatase form, with an average size of 8.1 nm, was detected from its XRD pattern (Fig. 3). The bulk Zr/Ti ratio determined by ICP-MS was 0.09, whereas the surface Zr/Ti ratio analyzed by XPS was 0.32. The larger surface Zr/Ti ratio indicates that the Zr⁴⁺ ions were mainly incorporated in the surface layers rather than in the bulk. Moreover, the bulk Zr/Ti ratio was less than the added value (Zr/Ti = 0.67) in the synthesis medium because of the faster kinetics of condensation between the Ti species. The IR spectrum of the Zr-doped TiO₂ shows C–H and P–O stretching absorptions at 2800–3000 and 1091 cm^{−1}, respectively (Fig. 2), indicating that the TOPO was chemically bound to the surface through the formation of P–O–Ti bonds. In addition, TOPO exhibited an increase in the binding energy of its P 2p state from 130.27 to 132.00 eV in the Zr-doped TiO₂ (Fig. 3), suggesting deformation of the R₃P=O functional groups into R₃P–O–M bonds. This result is in agreement with the finding in the FTIR spectrum.

3.2. Thermal analysis

The thermal behavior of TOPO-capped nanocrystals was analyzed using TGA/DSC. Fig. 1 displays the weight loss and heat flow of the TOPO-capped Zr-doped TiO₂ in air. An endothermic process (centered at 70 °C) accompanied by a 3.4% weight loss

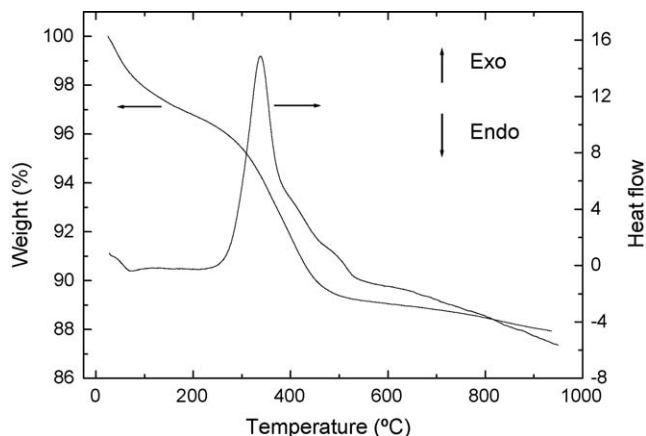


Fig. 1. The TGA/DSC curves of the TOPO-capped Zr-doped TiO₂ heated in air.

occurred when the temperature increased from room temperature to 228 °C, denoting the elimination of adsorbed water. At 228–550 °C, a significant weight loss of 7.45% with an exothermic peak centered at 337.6 °C was observed. These results indicate the pyrolysis and gasification of the alkyl chains of TOPO. A slight weight loss of 1.17% took place at 550–950 °C, corresponding to thermally induced dehydroxylation or deoxygenation at high temperature.

3.3. Surface properties

To understand the thermal induced changes in surface chemical species, the samples calcined at various temperatures were analyzed using FTIR and XPS. Fig. 2 shows the FTIR spectra of the TOPO-capped Zr-doped TiO₂ calcined at elevated temperatures. The C–H stretching absorption (2768–2981 cm^{−1}) which was obvious in the TOPO-capped samples disappeared after calcination at 250 °C. Instead, C=C or C=O stretching modes at 1320–1790 cm^{−1} were observed [11], indicating thermal induced partial oxidation and pyrolysis of TOPO. The carbonaceous absorptions were not detectable at 450 °C, indicating that the surface carbons were almost completely removed by calcination. Meanwhile, the calcined samples began to show OH bending and stretching absorptions at 1613 and 3285 cm^{−1}, respectively [12]. Similar absorptions blue-shifted to 1625 and 3393 cm^{−1}, respectively, at 550 °C. The higher bonding strength after calcination at higher temperature reveals that reductive conditions resulted from dehydroxylation and/or deoxygenation. The OH absorptions diminished gradually for the samples calcined above 750 °C and disappeared at 950 °C. Two absorption bands at 1031–1082 and 1127–1192 cm^{−1} corresponding to antisymmetric/symmetric O–P–O stretching modes appeared for the samples calcined above 450 °C [13,14]. The shifts of these bands suggest that different chemical environments existed around the phosphorus elements after calcination at the various temperatures. To understand the chemical structures of the phosphorus species, we used XPS to further characterize the chemical states and relative elemental ratios of the calcined samples.

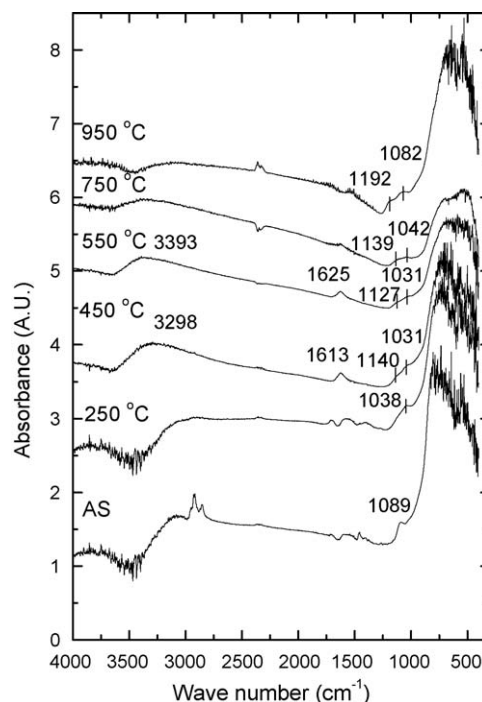


Fig. 2. The FTIR spectra of the TOPO-capped Zr-doped TiO₂ calcined at various temperatures.

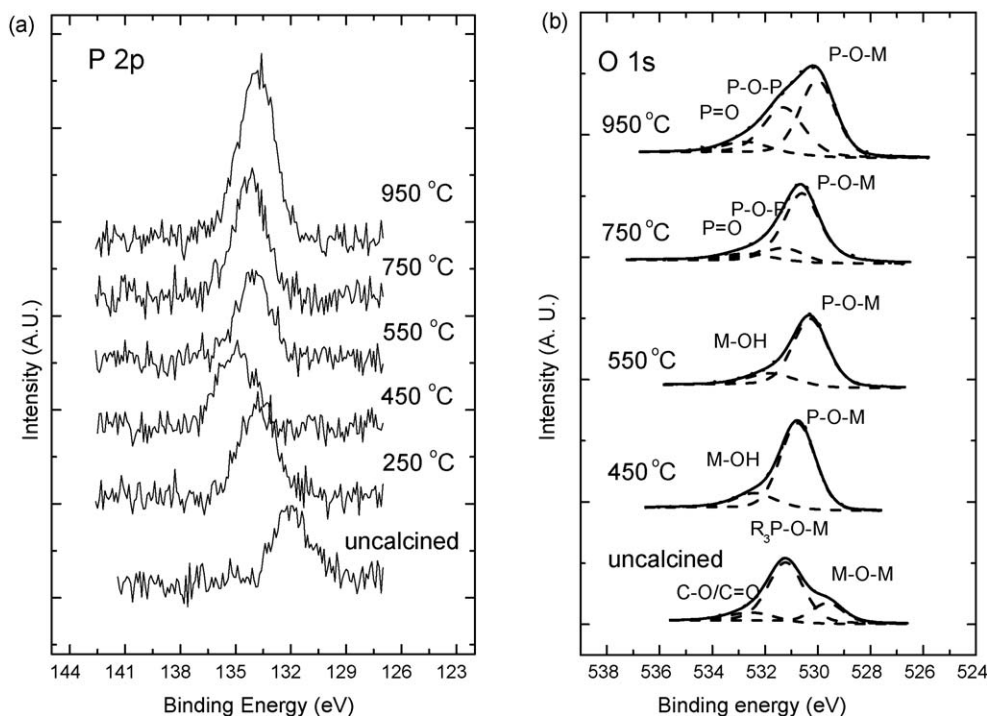


Fig. 3. The P 2p and O 1s XP spectra of the TOPO-capped Zr-doped TiO_2 calcined at various temperatures. The experimental results, the fitted peaks, and the summarized results of the fitted data are presented as dotted, dashed, and solid curves, respectively.

Fig. 3 displays the XP spectra of the P 2p and O 1s states of the TOPO-capped Zr-doped TiO_2 calcined at various temperatures. Oxidation of the bonded TOPO resulted in a chemical shift of the P 2p states from 132.00 to 133.88 eV at 250 °C. The highest binding energy for the P 2p peak occurred at 134.80 eV for the sample calcined at 450 °C. This binding energy is even higher than that of PO_4^{3-} units (133.7 ± 0.2 eV) [8], suggesting that the P^{5+} ions have a penta-coordinated bonding configuration. For the samples calcined at 550–950 °C, the binding energy of the P 2p peak decreased to 133.87–134.10 eV, indicating the formation of phosphated Zr-doped TiO_2 at the high temperatures.

The O 1s spectra of the calcined and uncalcined samples can be curve fitted into several states. The TOPO-capped nanocrystals contained M–O–M (529.63 eV, M = Ti or Zr), $\text{R}_3\text{P–O–M}$ (531.21 eV), and C–O or C=O states (532.52 eV) [8]. The existence of the C–O/C=O state reveals partial decomposition of the alkyl chains of TOPO during synthesis. Calcination introduced P^{5+} ions into the surface lattice of the TiO_2 . The P–O–M state for the sample calcined at 450 °C exhibited the highest binding energy of 530.78 eV. Moreover, the surface $\text{O}_\text{M}/\text{M}_\text{S}$ ratio (where O_M denotes metal-bonded oxygen ions and M_S means the sum of the Ti and Zr ions) exhibited the highest value of 2.22 at this temperature. These findings suggest that severe oxidation of carbons at 450 °C introduced a large number of oxygen ions into the surface lattice and resulted in the most oxidative conditions. This hypothesis is supported by the higher wavenumber of the signals for the OH groups in the FTIR spectrum and the higher binding energy of the P 2p state in the XP spectrum of the sample calcined at 450 °C. Deoxygenation reduced the $\text{O}_\text{M}/\text{M}_\text{S}$ ratio from 2.22 to 1.72 when the calcination temperature increased to 550 °C. In addition, the P–O–M states shifted to a lower binding energy of 530.31 eV. In turn, alternative P=O (532.75 eV) [15] and P–O–P (531.30 eV) [15] states comprising 7 and 13% of the phosphorous species, respectively, appeared for the sample calcined at 750 °C. The contents of the P=O and P–O–P units increased to 9 and 38%, respectively, when the sample was calcined at 950 °C. These results reveal that pyrophosphate moieties had formed and their content

increased upon increasing the calcination temperature. Yu reported similar results for TiP_2O_7 or $\text{TiO}_2(\text{P}_2\text{O}_7)$ formed in the P-doped TiO_2 at 800 °C [16]. The critical P/Ti ratio determining the formation of pyrophosphate species was 0.15. In this study, the surface $\text{P}/\text{M}_\text{S}$ ratios were 0.29 and 0.45 at 750 and 950 °C, respectively. These values are all higher than the critical ratio required to trigger the formation of pyrophosphate species.

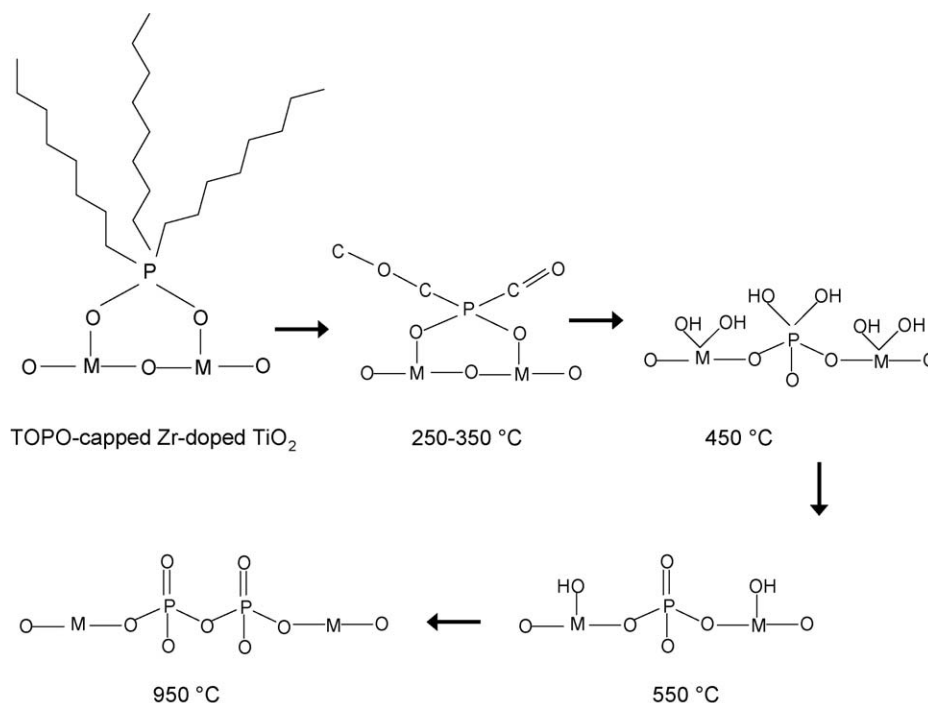
Table 1 shows the Zr/Ti, P/Ti, and $\text{O}_\text{M}/\text{M}_\text{S}$ ratios of the samples calcined at various temperatures. The bulk Zr/Ti and P/Ti ratios of the phosphated sample calcined at 950 °C were 0.08 and 0.03, respectively. These values are similar to those (Zr/Ti = 0.09, P/Ti = 0.02) of the TOPO-capped nanocrystals, indicating that both the Zr^{4+} and P^{5+} ions were non-volatile during thermal treatment. The surface Zr/Ti and P/Ti ratios were in the range of 0.32–0.41 and 0.27–0.62, respectively. These values were 5–31 times higher than those in the bulk. Thus, the Zr^{4+} and P^{5+} ions both accumulated mainly in the surface lattice rather than being doped in the bulk during calcination. In addition, the P/Ti ratio increased remarkably from 0.40 to 0.62 as the calcination temperature increased from 750 to 950 °C. The corresponding crystallite sizes of the samples grew significantly from 10.2 to 16.1 nm. These results suggest the segregation of P^{5+} ions from intersectional regions of the grains during coalescence of the nanocrystals. Such segregation of Zr^{4+} ions was not efficient, however, because the changes in the Zr/Ti ratio were insignificant upon increasing the calcination tempera-

Table 1

The Zr/Ti, P/Ti, and $\text{O}_\text{M}/\text{M}_\text{S}$ ratios of the TOPO-capped and phosphated Zr-doped TiO_2 calcined at varies temperatures.

Calcination	Temp.	Uncalcined	450	550	750	950
Zr/Ti	XPS	0.32	0.35	0.41	0.40	0.39
	ICP-MS	0.09	— ^a	— ^a	— ^a	0.08
P/Ti	XPS	0.33	0.27	0.33	0.40	0.62
	ICP-MS	0.02	— ^a	— ^a	— ^a	0.03
$\text{O}_\text{M}/\text{M}_\text{S}$	XPS	— ^a	2.22	1.72	1.48	1.38

^a Not detected.



Scheme 1. Surface phosphation through calcination of TOPO-capped nanocrystals at various temperatures.

tures. As the result, some of the Zr^{4+} ions were incorporated into the bulk TiO_2 lattice during fusion of the nanocrystals. We attribute the low solubility of the P^{5+} ions in the TiO_2 to their small ionic radius (0.38 Å), which is 44% lower from that of Ti^{4+} (0.68 Å) [17]. Dehydroxylation and deoxygenation reduced the $\text{O}_\text{M}/\text{M}_\text{S}$ ratio from 2.22 to 1.38 when the calcination temperature increased from 450 to 950 °C. The non-stoichiometry of the phosphated Zr-doped TiO_2 indicates unsaturated coordination of their Ti^{4+} or Zr^{4+} ions. In addition, the number of oxygen vacancies increased with increasing temperature.

Based on the FTIR spectra and XPS data, we developed a mechanism for the phosphation of the Zr-doped TiO_2 during calcination of the TOPO-capped nanocrystals. Scheme 1 shows the phosphation process occurring at elevated calcination temperatures. The chemically bonded TOPO was initially pyrolyzed through thermal treatment in air at 250–350 °C. Severe oxidation at 450 °C not only removed the organic carbons but also introduced many oxygen ions into the TiO_2 surface lattice. Penta-coordinated P^{5+} ions were formed initially under the oxidation conditions. Dehydroxylation and deoxygenation reduced the amounts of O^{2-} ions and resulted in PO_4^{3-} at 550 °C. Further increases in temperature led to progressive concentration of the surface PO_4^{3-} species through a segregation process. Condensation of the PO_4^{3-} units resulted in the formation of pyrophosphate species above 750 °C.

3.4. Microstructures

Fig. 4 shows the HRTEM images of the TOPO-capped Zr-doped TiO_2 nanocrystals before and after calcination at 450, 750, and 950 °C. The sample calcined at 450 °C still exhibited faceted rods, having length and width of ca. 25.0 and 10.8 nm, respectively. Most of the faceted nanorods maintained their shapes and single-crystallinity up to 750 °C, although a few large particles with irregular shapes were generated (Fig. 4c and e). The nanorods grew into large spherical grains (diameter of ca. 20 nm) that were imbedded in micrometer-sized particles when the phosphated Zr-doped TiO_2 was calcined at 950 °C. Fused crystal boundaries were clearly evident in its high-magnification TEM image (Fig. 4f).

The specific surface areas of the samples calcined at 450 and 550 °C were 112 and 114 m^2/g , respectively. Relative to the low specific surface area of the TOPO-capped Zr-doped TiO_2 (0.5 m^2/g), these great increases in the specific surface area after calcination were due to the removal of the surface organic moieties and reduced hydrophobic interactions between the nanocrystals. When the temperature increased to 750 °C, heat-induced coalescence between particles reduced the specific surface area of the phosphated samples to 57 m^2/g . An even smaller specific surface area of 2.4 m^2/g was obtained after calcination at 950 °C because of increased particle sizes.

We used XRD to further examine the average crystalline properties of the phosphated Zr-doped TiO_2 . Fig. 5 displays the XRD patterns of the TOPO-capped Zr-doped TiO_2 before and after calcination at various temperatures. The anatase form was dominant in all of the samples, even after calcination at 950 °C. We did not detect any ZrTiO_4 or TiP_2O_7 species because of their low concentrations. The crystallite sizes of the anatase crystals were estimated from the broadening of the (1 0 1) diffraction peak using Scherrer equation. The samples exhibited average crystallite sizes of 10.2–10.8 nm at 250–750 °C. A significant increase in the crystallite sizes (to 16.1 nm) was obtained at 950 °C. The surface Zr^{4+} and P^{5+} ions prevented the coalescence/growth of the TiO_2 crystals because they resulted in mismatched microstructures in the grain boundaries. The inhibition of the growth of the anatase crystals also maintained the anatase metastability at high temperature. Reidy et al. [18] reported that the critical sizes for 1 and 25% anatase-to-rutile conversion were 37.5 and 45.1 nm, respectively. In this study, the largest crystallite size of the phosphated Zr-doped TiO_2 was 16.1 nm, i.e., it was too small to undergo phase transformation. In addition, the (1 0 1) diffraction peak shifted from a 2θ position of 25.18° to 25.09° when the calcination temperature increased from 750 to 950 °C, indicating an expanded d-spacing. This situation arose as the result of the incorporation of Zr^{4+} ions, which have a larger ionic radius (0.79 Å) than Ti^{4+} (0.68 Å), into the bulk lattice. The presence of these lattice impurities (Zr^{4+} ions) also assisted in maintaining the high stability of the anatase phase.

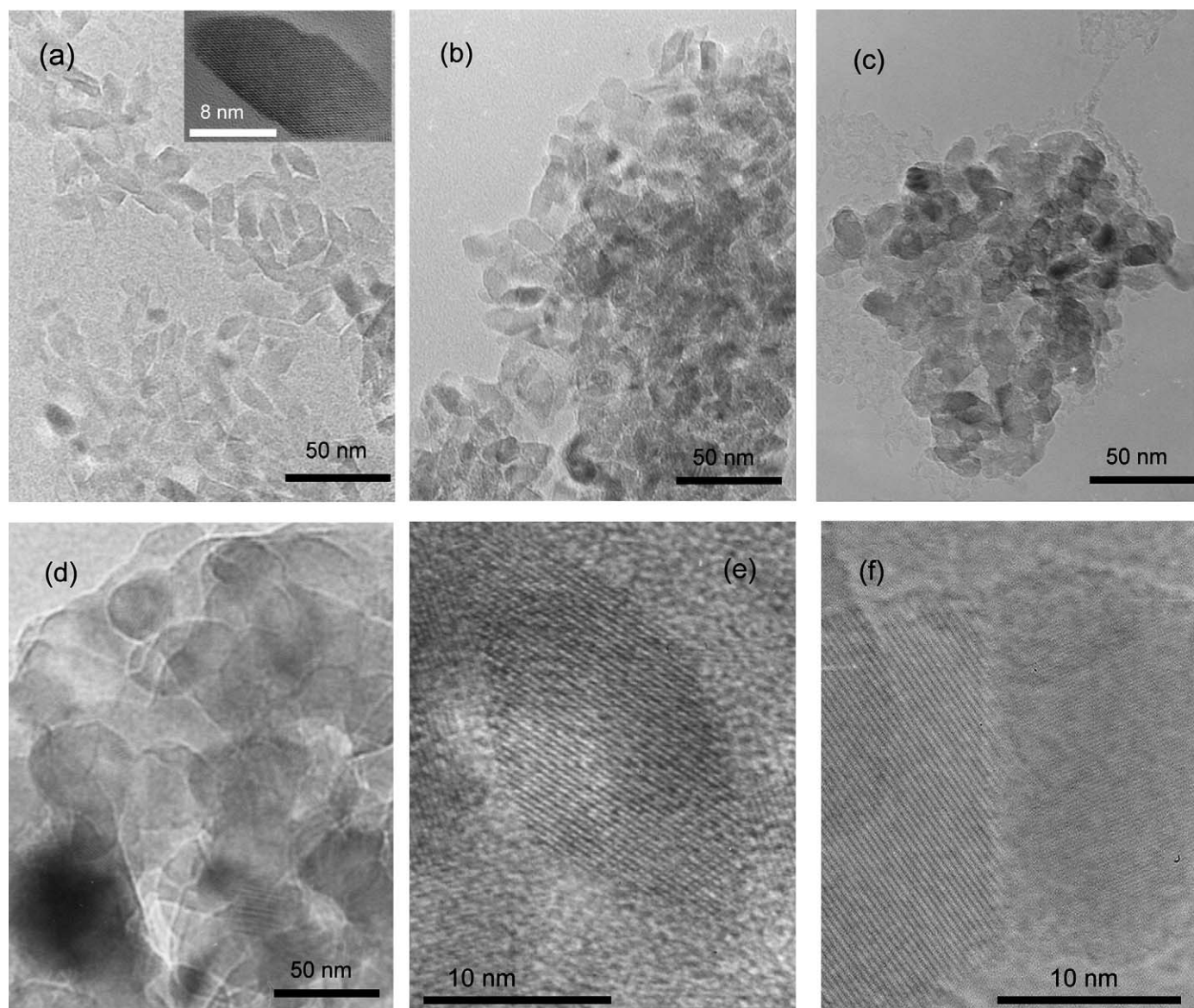


Fig. 4. The HRTEM images of (a) the as-prepared TOPO-capped Zr-doped TiO₂ and (b–d) the samples obtained after calcination at (b) 450 °C, (c) 750 and (d) 950 °C. (e, f) The high-magnification images of (c) and (d), respectively.

The bandgaps of the samples calcined at 250–750 °C were 3.4 eV. Introducing Zr⁴⁺ and P⁵⁺ ions does not reduce the bandgap of TiO₂ because the location of the energy states of the Zr⁴⁺ and P⁵⁺ ions are located in the conduction and valence band regions,

respectively [5,7]. The bandgap declined to 3.2 eV at 950 °C, however, mainly because of the increase in the crystallite sizes.

3.5. Photocatalytic activity

The photocatalytic activities of the phosphated Zr-doped TiO₂ and P25 were examined in terms of the decomposition of BPA at 20 mg/l. The phosphated Zr-doped TiO₂ at 550 °C ($k_{app} = 1.17 \times 10^{-1} \text{ min}^{-1}$) exhibited the highest apparent catalytic activity, followed by the photocatalysts at 750 or 450 °C ($k_{app} = 1.07 \times 10^{-1} \text{ min}^{-1}$) and then the sample at 950 °C ($k_{app} = 3.37 \times 10^{-2} \text{ min}^{-1}$). Compared to the degradation by P25 ($k_{app} = 1.78 \times 10^{-2} \text{ min}^{-1}$), the phosphated Zr-doped TiO₂ at 550, 750/450, and 950 °C exhibited 6.6, 6.0, and 1.9-fold increases, respectively, in the apparent photocatalytic activities (see [Supplementary materials, Fig. S1](#)). The high activities at 450–550 °C are mainly due to high specific surface areas. To understand the surface activities of the phosphated Zr-doped TiO₂, we normalized the apparent rate constants with specific surface areas of the photocatalysts. [Fig. 6](#) shows the specific rate constants for the degradation of BPA by P25 and the phosphated Zr-doped TiO₂

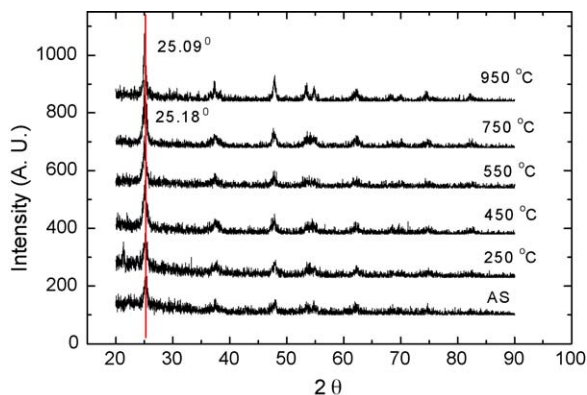


Fig. 5. The XRD patterns of the TOPO-capped Zr-doped TiO₂ before and after calcination at various temperatures.

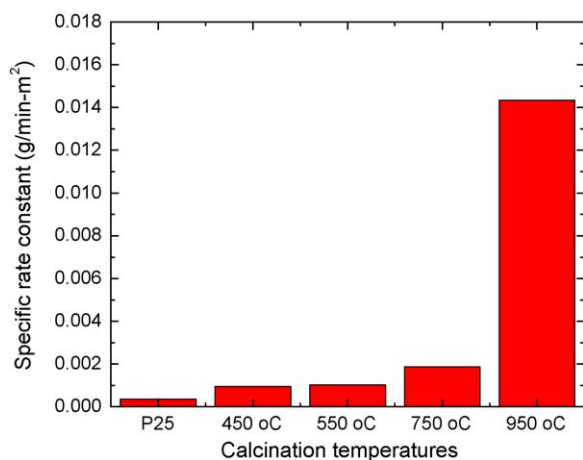


Fig. 6. The specific rate constants for the degradation of BPA by P25 and the phosphated Zr-doped TiO₂ calcined at various temperatures.

calcined at various temperatures. The catalysts that had been calcined at 950, 750, 550, and 450 °C exhibited specific rate constants of 1.43×10^{-2} , 1.88×10^{-3} , 1.03×10^{-3} and 9.52×10^{-4} g/min-m², respectively, which were 40.3, 5.28, 2.88, and 2.67 times higher, respectively, than that of P25 (3.56×10^{-4} g/min-m²). Therefore, the phosphated Zr-doped TiO₂ exhibited increased photocatalytic activity upon increasing the calcination temperature. To the best of our knowledge, the extraordinarily high photocatalytic activity of the phosphated Zr-doped TiO₂ calcined at 950 °C is higher than that of any other reported doped TiO₂. We attributed this great enhancement to the chemical compositions, microstructures and surface hydrophobicity of this sample.

The introduction of defects via the incorporation of impurities into TiO₂ lattice generally enhances the photocatalytic activity as a result of retardation of charge recombination [19]. Relative to bulk defects, surface defects contribute more to the kinetics of photocatalysis because they not only prolong the charge lifetime (by trapping the charge carriers) but also transfer the trapped charges to reactants. In a previous paper, we reported the higher photocatalytic activity of Zr-doped TiO₂ over those of pure TiO₂ and P25 [3]. In this study, we used a non-hydrolytic sol-gel method to incorporate Zr⁴⁺ ions into the surface lattice of TOPO-capped TiO₂ nanocrystals and then introduced P⁵⁺ ions into the surface lattice through calcination of the TOPO-capped nanocrystals. Similarly, Stone and Davis [20] prepared a TiO₂ molecular sieve using a phosphorous-containing ligand, dodecyl phosphate, as the template and doped P⁵⁺ ions into the TiO₂ lattice through calcination. They observed, however, a low photocatalytic activity for the P-doped TiO₂. They attributed the limitation to a high concentration of defects resulted from the P⁵⁺ ions which induced charge recombination. Körösi et al. [8] reported that phosphated TiO₂ having surface P/Ti ratios ranging between 0.12 and 0.22 exhibited the highest efficiency for the conversion of ethanol to CO₂. In this study, the surface P/Ti ratios of the phosphated Zr-doped TiO₂ were in the range of 0.27–0.62, considerably higher than the reported optimal values, therefore suggesting the coexistence of Zr⁴⁺ ions play a crucial role in the high photocatalytic activity of the phosphated samples. We used the similar procedure (NHSG followed by calcination) to prepare phosphated TiO₂ at 550 °C. Its rate constant for the decomposition of BPA was 2.36×10^{-4} g/min-m². This value was lower than that of the corresponding phosphated Zr-doped TiO₂. In addition, it was also lower than that of P25. This result provides clear evidences that co-existence of Zr⁴⁺ and phosphate ions in the surface lattice of TiO₂ is the key feature affecting its high surface reactivity. Co-

doping has been demonstrated previously to improve the photocatalytic activity of TiO₂ [21,22]. Miyauchi et al. [21] reported that the SrTiO₃ co-doped with La³⁺ and N³⁻ exhibited a higher rate of oxidation for 2-propanol under illumination with visible light than that of the corresponding sample doped only with N³⁻. This improved activity was attributed to decreases in oxygen vacancies caused by charge compensation. Liu et al. [23] incorporated N³⁻ and Ce⁴⁺ ions into TiO₂ to enhance its photocatalytic activity under irradiation with visible light. The improvement arose because N-doping narrowed the band gap of TiO₂ to increase the absorption of visible light. In addition, the Ce⁴⁺ ions served as electron trapping centers, thereby reducing charge recombination. In our present study, the existence of the co-dopant, Zr⁴⁺, introduced alternative defect levels close to the conduction band of TiO₂ [5]. These Zr⁴⁺ ions can act as electron trap centers to inhibit charge recombination. In addition, unoccupied P 3p energy levels located in the low energy region of the valence band can promote the oxidation of BPA because of their high reduction potential. Although co-doping of Zr⁴⁺ and P⁵⁺ ions resulted in less reduction on the band gap of TiO₂, their moderate energy levels maintained the charge lifetime and facilitated interfacial charge transfer for high photocatalytic activity.

We found that calcination at elevated temperatures changed the surface compositions and microstructures and progressively improved the photocatalytic activity of the phosphated Zr-doped TiO₂. A remarkable 14-fold enhancement of the specific rate constant resulted when we increased the temperature from 550 to 950 °C. In addition, the crystallite size of the doped TiO₂ grew to 16.1 nm when the sample was calcined at 950 °C. This size is close to the reported optimal size (15.0 nm) at which an anatase TiO₂ exhibited the highest photocatalytic activity because volume and surface charge recombination was minimum and interfacial charge transfer was maximized [24]. Because approaching the optimal value only doubled the activity of the TiO₂ at most [24], we believe that, in this study, the surface properties dominated the extremely high surface reactivity of the sample calcined at high temperature more than the crystallite structures.

3.6. Adsorptions

Surface properties play crucial roles in the adsorption of reactants onto photocatalysts and interfacial charge transfer; therefore they control surface reactivity. Segregation and condensation of phosphate species resulted in the formation of pyrophosphate species at temperatures above 750 °C. Moreover, dehydroxylated surface was obtained at high temperature. To understand the affinity of the dehydrated photocatalysts prepared through calcination at 950 °C toward BPA, we examined the adsorption isotherm of the target compound in the dark. Fig. 7 shows the amount of adsorbed BPA on TiO₂ (*Q*, mg/g) against its equilibrium concentrations (*C_e*, mg/l) in aqueous solution. The adsorbed amounts increased to 3.85 mg/g upon increasing the equilibrium concentration of BPA to 26.15 mg/l. Heterogeneous adsorption is generally described by the Langmuir model which can be expressed as following equation:

$$\frac{C_e}{Q} = \frac{1}{X_m K} + \frac{1}{X_m} C_e \quad (1)$$

where *X_m* (mg/g) denotes the maximum adsorbed capacity on the photocatalysts and *K* (l/mg) is the energy-dependent adsorption coefficient. The inset in Fig. 7 shows the linear fit of the plot of *C_e/Q* versus *C_e*. The phosphated Zr-doped TiO₂ provided values of *X_m* and *K* of 5.35 mg/g and 14.05 l/mg, respectively, for the adsorption of BPA. In contrast, P25 exhibited insignificant adsorption for BPA. This result evidences that the dehydrated TiO₂ has higher adsorption ability toward this hydrophobic compound than does

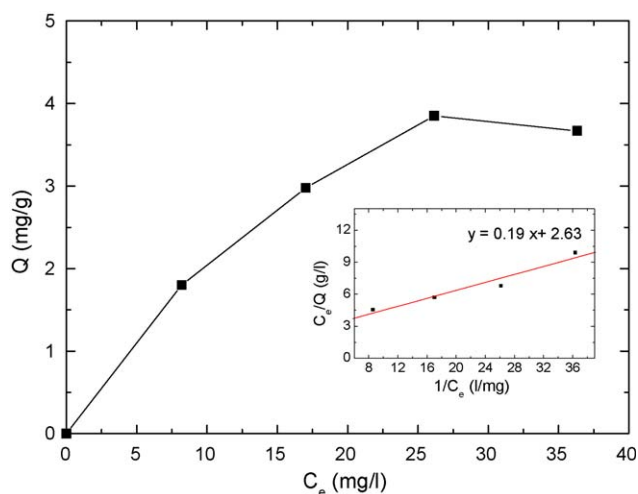


Fig. 7. The dark adsorption isotherm for BPA in the suspension of the phosphated Zr-doped TiO_2 that had been calcined at 950°C . Inset shows the linear fit of the experimental data obtained using the Langmuir isotherm model.

the hydrated one. Such affinity improves the mass transfer of BPA from the bulk solution to the surface of the photocatalysts, thereby enhancing the photocatalytic activity. Nosaka et al. [25] compared the photocatalytic activity of hydrated P25 and dehydrated TiO_2 for the decomposition of benzoic acid. Similarly, they found that the reaction performed on the dehydrated TiO_2 was much more efficient than that on the hydrated one. Thus, it appears that the dehydrated surface has higher adsorbability toward the hydrophobic compound and selectively initiates direct photocatalysis.

It has been reported that the adsorption ability of TiO_2 is altered after irradiation because of changes induced in the surface electronic properties [26]. We further investigated photo-induced adsorptions of the modified TiO_2 by determining the initial degradation rates of BPA under different initial concentrations of the target compound (see [Supplementary materials, Fig. S2](#)). According to the linear Langmuir-Hinshelwood model, the surface-modified TiO_2 provided an intrinsic rate constant (k_r) and a pseudo-equilibrium adsorption constant (K_a) of $4.70 \times 10^{-1} \text{ mg-g/l-min-m}^2$ and $5.13 \times 10^{-2} \text{ l/mg}$, respectively. The corresponding values in the P25-based system were $5.79 \times 10^{-2} \text{ mg-g/l-min-m}^2$ and $9.27 \times 10^{-3} \text{ l/mg}$, respectively. Compared with the commercial product P25, the higher intrinsic rate constant and adsorption coefficient of the phosphated Zr-doped TiO_2 indicate that it possessed a higher quantity of effective charges and underwent more efficient chemisorption. On the other hand, the pseudo-equilibrium constant K_a of the modified sample was 3.66×10^{-3} times smaller than its K (14.05 l/mg) measured in the dark. Differences between adsorption coefficients determined in the dark and under illumination have also been found for benzyl phenol, 4-chlorophenol, and metobromuron [26,27]. These systems, however, exhibited larger photoadsorption constants than those obtained in the dark. In this study, the lower pseudo-equilibrium constant suggests that photo-induced adsorption of water hindered or repelled the attachment of BPA onto the surface of the phosphated Zr-doped TiO_2 . We believed that pyrophosphate species increases the Lewis acidity of TiO_2 relative to that of phosphate species. Therefore, the strong Lewis acid sites either readily chemisorb water to generate reactive hydroxyl radicals for efficient mediated photocatalysis [28], or they promote the chemisorption of BPA for rapid direct photocatalysis. After photocatalysis, the phosphated Zr-doped TiO_2 exhibited the binding energy of its P 2p state centered at 133.8 eV and a P/Ti ratio of 0.60 (see [Supplementary materials, Fig. S3](#)). These results were similar to those (P 2p at 133.9 eV , P/Ti = 0.62) obtained before

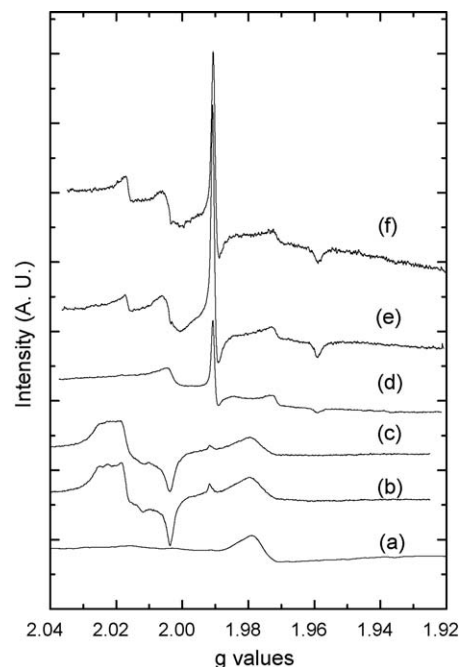


Fig. 8. EPR spectra of (a) P25 that had been treated under vacuum at 120°C for 1 h, (b) the P25 irradiated at 77 K under vacuum, (c) the P25 irradiated at 77 K under an O_2 atmosphere, (d) the 950°C -calcined phosphated Zr-doped TiO_2 that had been treated under vacuum at 120°C for 1 h, (e) the phosphated Zr-doped TiO_2 irradiated at 77 K under vacuum, and (f) the phosphated Zr-doped TiO_2 irradiated at 77 K under an O_2 atmosphere. All the spectra were acquired at 77 K.

photocatalysis, indicating the high stability of the incorporated pyrophosphate ions against photocorrosion.

Oxygen molecules served as electron scavengers in our photocatalytic systems. Interfacial charge transfer from electron-trapped sites to adsorbed O_2 is considered to be the rate determining step in the kinetics of photocatalysis [29]. To understand whether the phosphated Zr-doped TiO_2 calcined at 950°C promoted the charge transfer, we determined the changes in the quantity of photogenerated electrons before and after exposure of O_2 using EPR. [Fig. 8](#) shows the EPR spectra of the phosphated Zr-doped TiO_2 and P25 recorded in the dark or under illumination in vacuum or under O_2 at 77 K. All the intensities of the EPR signals were normalized with respect to the surface areas of the photocatalysts. The phosphated Zr-doped TiO_2 in the dark contained a remarkable set of g-values at $g_{\perp} = 1.991$ and $g_{\parallel} = 1.962$ which corresponded to Ti^{3+} centers [30]. In addition, a small signal at $g_{\perp} = 1.972$ was assigned to distorted Ti^{3+} sites [31]. These results indicate that a reduced TiO_2 surface arose from dehydroxylation/deoxygenation at high temperature. The g value at 2.003 represented the $\text{Ti}^{4+}\text{-O}_2^-$ superoxide species that formed by chemisorption of O_2 with Ti^{3+} centers [32]. After illumination with UV light, an additional signal at $g = 2.017$ was detected, denoting trapped holes at surface O^- sites [32]. Moreover, the intensities of the signals of the trapping photogenerated electrons at Ti^{3+} centers dramatically increased from 6385 to 18,638 a.u. After adding O_2 , the irradiated phosphated Zr-doped TiO_2 showed decreased Ti^{3+} signals (15,075 a.u.), which was 3563 a.u. lower than those measured under vacuum. This phenomenon indicates that electron transfer occurred from Ti^{3+} sites to O_2 . In contrast, the spectrum of P25 did not show $\text{Ti}^{4+}\text{-O}_2^-$ superoxide species, revealing that the chemisorption of O_2 on the surface of P25 was insignificant. Moreover, exposure to O_2 reduced the intensity of its Ti^{3+} signals only by 414 a.u. These findings indicate that interfacial electron transfer in the phosphated Zr-doped TiO_2 is more efficient than that in P25.

Henderson et al. [33] reported that chemisorption of O₂ molecules is forbidden on fully oxidized surface which does not contain vacancies. In this study, we found that thermally induced dehydroxylation and deoxygenation resulted in large amounts of oxygen vacancies in the samples calcined at 950 °C (O_M/M_S = 1.38). The oxygen deficient surface helps adsorption of oxygen either in molecular or dissociated forms and facilitates interfacial charge transfer. The sites for the adsorption of O₂ are generally blocked in the presence of adsorbed water on the surface [34]. In this study, we obtained a dehydrated surface for the pyrophosphated Zr-doped TiO₂ calcined at high temperature. Attwood et al. [34] used EPR to analyze the life time of oxygen radicals on hydrated and dehydrated titania surface and found that O₂^{•−} was more prominent and longer lasting on the dehydrated surface. However, the dehydrated surface of sol–gel-derived metal oxide and P25 is not accessible because of the rapid recovery of water during cooling [35]. Nosaka et al. [25] claimed that the TiO₂ presenting terminal hydroxyl groups readily rehydrate via dissociative adsorption of water. In contrast, thermal desorption of bridged hydroxyl groups leads to incompletely coordinated sites where recovery of water is not available. In this study, the surface of the non-hydrolytic sol–gel-derived TiO₂ lacked of terminal hydroxyl groups because water was not involved in the cross-condensation between TiCl₄ and Zr(OC₃O₇)₄. Therefore, permanent dehydration of the TiO₂ can be obtained after heating at 950 °C. The modified surface electronic structures, acidity, dehydrated properties, and crystalline structures cause synergetic contributions leading to the extraordinary activity of the phosphated Zr-doped TiO₂ calcined at high temperature.

4. Conclusions

Incorporation of phosphate/pyrophosphate species into surface lattice of Zr-doped TiO₂ is achieved through calcination (>550 °C) of TOPO-capped nanocrystals that had been derived from a non-hydrolytic sol–gel manner. The coexistence of Zr⁴⁺ ions and phosphate/pyrophosphate species result in the TiO₂ exhibiting higher photocatalytic activities than that of commercial product P25 for the decomposition of BPA. The Zr⁴⁺ ions with energy levels in the conduction band trap electrons to reduce charge recombination, while the P⁵⁺ ions having energy levels in the lower valence band region promote the oxidation of the target compounds for efficient photocatalysis. Calcination at elevated temperatures improves the photocatalytic activity. The surface-doped TiO₂ calcined at 950 °C exhibits a photocatalytic activity that is 40.3 times higher than that of P25. This improvement is mainly due to thermally induced changes in the surface properties. Pyrophosphate species, which is formed through segregation and condensation of phosphate species, increases surface Lewis acidity. Moreover, dehydrated and oxygen deficient surface is obtained by dehydroxylation and deoxygenation. Such a surface structure favors the chemisorption of O₂ and BPA and facilitates interfacial charge transfer. These synergetic effects contributed by co-doping, dehydration, oxygen deficiency, and existence of pyrophosphate species result in the extraordinarily high photocatalytic activity of the sample calcined at high temperature. In addition, they suggest that the phosphated Zr-doped TiO₂ hold great promise for the

advanced decomposition of endocrine disrupting chemicals which predominantly exhibit high hydrophobicity.

Acknowledgements

We thank the National Science Council, Taiwan, R.O.C. under grant No. NSC97-2221-E-009-044-MY2 and the MOE ATU Program for supporting this study financially.

Appendix A. Supplementary data

Supplementary data associated with this article can be found, in the online version, at doi:10.1016/j.apcatb.2009.03.009.

References

- [1] K. Ikeue, H. Yamashita, M. Anpo, T. Takewaki, *J. Phys. Chem. B* 105 (2001) 8350–8355.
- [2] X.T. Shen, L.H. Zhu, G.X. Liu, H.W. Yu, H.Q. Tang, *Environ. Sci. Technol.* 42 (2008) 1687–1692.
- [3] S.M. Chang, R.A. Doong, *J. Phys. Chem. B* 110 (2006) 20808–20814.
- [4] J.C. Yu, L.Z. Zhang, Z. Zheng, J.C. Zhao, *Chem. Mater.* 15 (2003) 2280–2286.
- [5] K. Nagaveni, M.S. Hegde, G. Madras, *J. Phys. Chem. B* 108 (2004) 20204–20212.
- [6] J. Lukac, M. Klementova, P. Bezdicka, S. Bakardjieva, J. Subrt, L. Szatmary, Z. Bastl, *J. Jirkovsky, Appl. Catal. B-Environ.* 74 (2007) 83–91.
- [7] K. Yang, Y. Dai, B. Huang, *J. Phys. Chem. C* 111 (2007) 18985–18994.
- [8] L. Korosi, S. Papp, I. Bertotti, I. Dekany, *Chem. Mater.* 19 (2007) 4811–4819.
- [9] G. Colon, J.M. Sanchez-Espana, M.C. Hidalgo, J.A. Navio, *J. Photochem. Photobiol. A* 179 (2006) 20–27.
- [10] E. Ortiz-Islas, T. Lopez, R. Gomez, J. Navarrete, *J. Sol-Gel Sci. Technol.* 37 (2006) 165–168.
- [11] S. SerghiniMonim, P.R. Norton, R.J. Puddephatt, *J. Phys. Chem. B* 101 (1997) 7808–7813.
- [12] M.P. Kapoor, S. Inagaki, H. Yoshida, *J. Phys. Chem. B* 109 (2005) 9231–9238.
- [13] A.I. Bortun, S.A. Khainakov, L.N. Bortun, D.M. Poojary, J. Rodriguez, J.R. Garcia, A. Clearfield, *Chem. Mater.* 9 (1997) 1805–1811.
- [14] Q.F. Wang, L. Zhong, J.Q. Sun, J.C. Shen, *Chem. Mater.* 17 (2005) 3563–3569.
- [15] Handbook of X-ray Photoelectron Spectroscopy: Perkin-Elmer Corporation, Physical Electronics Division, 1992.
- [16] H.F. Yu, *J. Mater. Res.* 22 (2007) 2565–2572.
- [17] P. Wu, Y.Z. Zeng, C.M. Wang, *Biomaterials* 25 (2004) 1123–1130.
- [18] D.J. Reidy, J.D. Holmes, M.A. Morris, *J. Eur. Ceram. Soc.* 26 (2006) 1527–1534.
- [19] W.Y. Choi, A. Termin, M.R. Hoffmann, *Angew. Chem. Int. Ed.* 33 (1994) 1091–1092.
- [20] V.F. Stone, R.J. Davis, *Chem. Mater.* 10 (1998) 1468–1474.
- [21] M. Miyauchi, M. Takashio, H. Tobimatsu, *Langmuir* 20 (2004) 232–236.
- [22] Y. Cong, J.L. Zhang, F. Chen, M. Anpo, D.N. He, *J. Phys. Chem. C* 111 (2007) 10618–10623.
- [23] C. Liu, X.H. Tang, C.H. Mo, Z. Qiang, *J. Solid State Chem.* 181 (2008) 913–919.
- [24] K.V. Baiju, S. Shukla, K.S. Sandhya, J. James, K.G.K. Warriar, *J. Phys. Chem. C* 111 (2007) 7612–7622.
- [25] A.Y. Nosaka, J. Nishino, T. Fujiwara, T. Ikegami, H. Yagi, H. Akutsu, Y. Nosaka, *J. Phys. Chem. B* 110 (2006) 8380–8385.
- [26] S. Parra, J. Olivero, C. Pulgarin, *Appl. Catal. B-Environ.* 36 (2002) 75–85.
- [27] A. Mills, S. Morris, *J. Photochem. Photobiol. A-Chem.* 71 (1993) 75–83.
- [28] R. Nakamura, T. Tanaka, Y. Nakato, *J. Phys. Chem. B* 109 (2005) 8920–8927.
- [29] M.R. Hoffmann, S.T. Martin, W.Y. Choi, D.W. Bahnemann, *Chem. Rev.* 95 (1995) 69–96.
- [30] C.P. Kumar, N.O. Gopal, T.C. Wang, M.S. Wong, S.C. Ke, *J. Phys. Chem. B* 110 (2006) 5223–5229.
- [31] D.C. Hurum, K.A. Gray, T. Rajh, M.C. Thurnauer, *J. Phys. Chem. B* 109 (2005) 977–980.
- [32] J.M. Coronado, A.J. Maira, J.C. Conesa, K.L. Yeung, V. Augugliaro, J. Soria, *Langmuir* 17 (2001) 5368–5374.
- [33] M.A. Henderson, W.S. Epling, C.L. Perkins, C.H.F. Peden, U. Diebold, *J. Phys. Chem. B* 103 (1999) 5328–5337.
- [34] A.L. Attwood, D.M. Murphy, J.L. Edwards, T.A. Egerton, R.W. Harrison, *Res. Chem. Intermed.* 29 (2003) 449–465.
- [35] S.M. Chang, R.A. Doong, *Chem. Mater.* 17 (2005) 4837–4844.